remote sensing

MDPI

Article

A Quantifying Approach to Soil Salinity Based on a Radar Feature Space Model Using ALOS PALSAR-2 Data

Nuerbiye Muhetaer, Ilyas Nurmemet *, Adilai Abulaiti, Sentian Xiao and Jing Zhao

Ministry of Education Key Laboratory of Oasis Ecology, College of Resources and Environmental Science, Xinjiang University, Urumqi 830046, China; nuerbiye@stu.xju.edu.cn (N.M.); adila@stu.xju.edu.cn (A.A.); 107552101062@stu.xju.edu.cn (S.X.); 107552101122@stu.xju.edu.cn (J.Z.)
* Correspondence: ilyas@xju.edu.cn

Abstract: In arid and semi-arid areas, timely and effective monitoring and mapping of salt-affected areas is essential to prevent land degradation and to achieve sustainable soil management. The main objective of this study is to make full use of synthetic aperture radar (SAR) polarization technology to improve soil salinity mapping in the Keriya Oasis, Xinjiang, China. In this study, 25 polarization features are extracted from ALOS PALSAR-2 images, of which four features are selected. In addition, three soil salinity inversion models, named the RSDI1, RSDI2, and RSDI3, are proposed. The analysis and comparison results of inversion accuracy show that the overall correlation values of the RSDI1, RSDI2, and RSDI3 models are 0.63, 0.61, and 0.62, respectively. This result indicates that the radar feature space models have the potential to extract information on soil salinization in the Keriya Oasis.

Keywords: soil salinization; polarized feature component; two-dimensional radar feature; Keriya Oasis

check for updates

Citation: Muhetaer, N.; Nurmemet, I.; Abulaiti, A.; Xiao, S.; Zhao, J. A Quantifying Approach to Soil Salinity Based on a Radar Feature Space Model Using ALOS PALSAR-2 Data. *Remote Sens.* **2022**, *14*, 363. https://doi.org/10.3390/rs14020363

Academic Editor: Abdul M. Mouazen

Received: 30 November 2021
Accepted: 10 January 2022
Published: 13 January 2022

Publisher's Note: MDPI stays neutral with regard to jurisdictional claims in published maps and institutional affiliations.

Copyright: © 2022 by the authors. Licensee MDPI, Basel, Switzerland. This article is an open access article distributed under the terms and conditions of the Creative Commons Attribution (CC BY) license (https://creativecommons.org/licenses/by/4.0/).

1. Introduction

Soil salinization is one of the most serious factors having a negative effect on agricultural sustainability and environmental health [1], causing the low emergence rate of crops, dwarf plants, and significant losses in soil fertility and exacerbating the desertification process [2–4]. Currently, more than 3% of global soil resources are affected by salt [5]. It is estimated that by 2050, the salinity of global arable land will reach more than 50% [6–8].

However, the situation in China seems to be more critical [9]. China alone is covered by 10% of the world's salinized land [10,11]. Xinjiang has the largest distribution of saline land in China, and its saline land accounts for 36.8% of the country, primarily at the oasis–desert ecosystem of southern Xinjiang (close to 50%) [12]. Thus, it is urgent to achieve regular and effective monitoring of soil salinity, which can provide effective support for decision making with regard to soil salinization control and more substantial information for soil remediation [13–18]. Soil salinity is not only very sensitive to variations in precipitation, temperature, and groundwater levels [2] but can also rapidly change after irrigation or precipitation. Meanwhile, a drought may cause salinity rates to increase in a matter of weeks [10].

Most of the traditional studies on soil salinization have been based on field sampling analysis technology, which is time-consuming and laborious and has a small spatial scale, fewer measurement points, and poor representative performance [14,19,20]. Remote sensing technology has great potential for the development of soil salinity prediction models because of its advantages of having a short revisit period, fast processing speed, and global coverage [2]. Therefore, optical remote sensing has played an important role in regional and even global soil salinization monitoring, mapping, and prevention [2,21]. Optical remote sensing has been the most widely used technique in multi-time dynamic monitoring of soil salinization distribution in large areas, and salinization inversion using the optical remote sensing interpretation technology has gradually been commenced.

However, optical remote sensing is difficult to perform under unstable weather conditions, and the lack of surface penetration capacity means that conventional optical remote sensing methods face different limitations in soil salinity monitoring [22,23]. Due to its all-day and all-weather earth observation capability without being affected by clouds and weather [22], high penetration capability, and sensitivity towards electrical conductivity (EC) [24–27], a synthetic aperture radar (SAR) can be effectively used in soil salinization monitoring applications [28]. Theoretically, SAR has great potential to investigate soil salinity [29]. Recent research has demonstrated that longer wavelengths provide a better capability to penetrate different soil types [30], such as S (2~4 GHz), L (1~2 GHz), and P (0.3~1 GHz) [23].

In a polarized SAR system, the information is contained in the electromagnetic waves received on the sensor that are reflected from the target object, which can be modulated in terms of spectrum, intensity, or electromagnetic waves [31]. Polarimetric synthetic aperture radar (PolSAR) represents an advanced imaging radar system, having a key role in radar remote sensing, namely, by using a PolSAR, more information can be obtained than by using a single-polarized regime radar [32–34]. The retention of more complete target polarization scattering characteristics makes PolSAR play an increasingly important role in acquiring numerous details of physical dielectric properties, geometry, and target orientation of ground objects, greatly enhancing the ability of radar to acquire target information [35]. Some researchers have taken advantage of the fact that the polarization parameters extracted by different polarization target decomposition methods are related to the physical properties of the ground objects [22], and they have broken down the PolSAR data and mined the hidden information to analyze and understand the scattering mechanisms of the ground objects [36,37]. Meanwhile, based on the polarization decomposition, the target features that conform to the classification conditions are extracted from the polarization SAR data, and then the classification and identification of the targets are realized [22,37]. The PolSAR has been widely used in many earth observation applications, including land cover monitoring [38–40], target detection [41–43], and terrain classification [44–47].

The polarization decomposition of a target has received great attention and achieved rapid development because it can reveal the scattering mechanism of the target and enhance the understanding of the target's scattering characteristics [48,49]. In addition, its polarization feature decomposition provides an effective tool for microwave remote sensing in the processes of saline land information extraction and salinity dynamics monitoring and can provide timely and effective guidance on agricultural production practices in arid areas [50].

The aim of this study is to construct a quantitative inversion model for radar remote sensing of soil salinity based on a two-dimensional radar feature space. The main procedures are as follows:

(1) Construction of a two-dimensional radar feature space based on optimal radar polarization feature components.
(2) Construction of a radar-based quantitative inversion model for soil salinity in a two-dimensional radar feature space.

2. Study Site and Data

2.1. Study Site

The study was carried out in the Keriya Oasis of southwestern Xinjiang, whose geographical position is between 36°44′59″–37°12′04″ N in latitude and 81°08′59″–82°00′03″ E in longitude [51]. The study area is located at the southern edge of the Taklamakan Desert and the north-central foothills of the Kunlun Mountains [32], which represents a typical oasis–desert intersection, as shown in Figure 1. The district falls under the arid regions of Hotan, covering an area of 3.95×10^4 km^2 [52]. The topography is higher in the south than in the north, and there is a 3500 m difference in height between the north and south [53]. The study area has a warm continental arid climate with low annual precipitation and high evaporation; the average multi-year precipitation is 44.7 mm, and the average multi-year evaporative energy is 2432.1 mm [53].

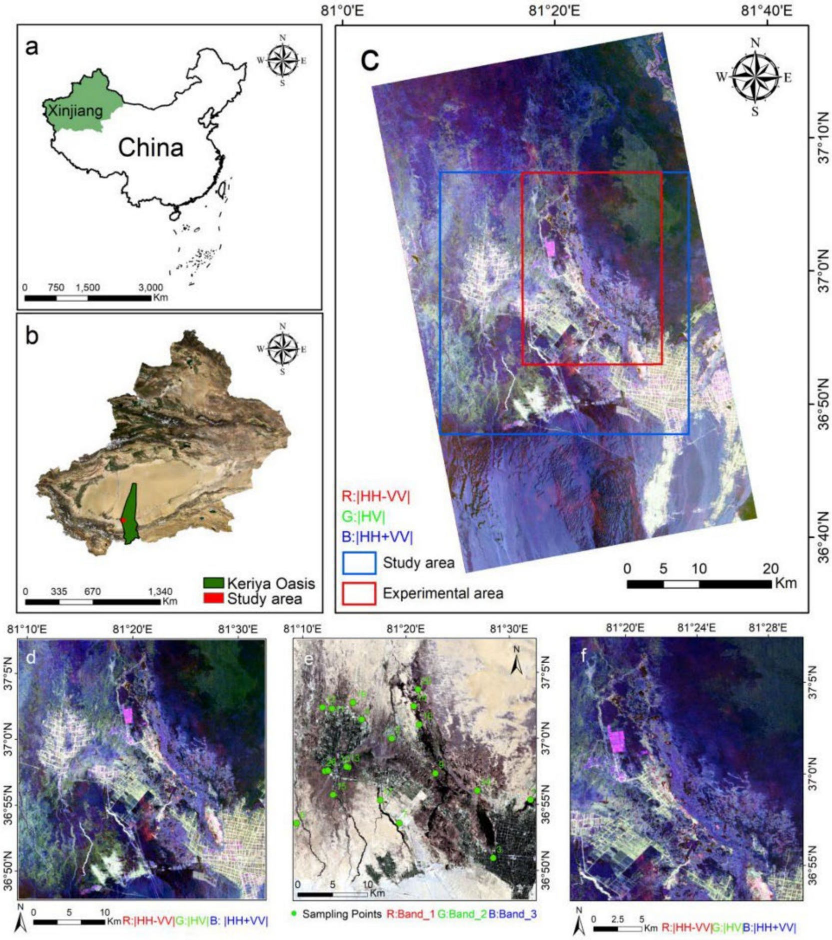

Figure 1. (**a**) Location of the study area on the overview map of China; (**b**) Xinjiang location; (**c**) the full phased array type L-band synthetic aperture radar (PALSAR-2) image; (**d**) the subset image covering the study area in Pauli decomposition with standard color-coding; (**e**) topographic map of sampling points of the study area; (**f**) typical land type in the experimental area.

The soil types of the study region are meadow soil and brown desert soil, and the soils are majorly distributed within areas of high groundwater mineralization and high water table [32]. The region under study entirely depends on the primary water source from the Keriya River, which is a seasonal river supplied by meltwater from glaciers and snow on the Kunlun Mountains and lost in the sands of the Taklimakan desert [54]. The major plants cultivated in the study region include cotton, wheat, corn, and rice [52]. As saline soils have a serious adverse impact on crop yields and agricultural production in the Keriya Oasis, effective monitoring of soil salinity in the early stages of salinization is essential to develop effective soil reclamation plans [32].

2.2. Data

2.2.1. Remote Sensing Data

The Advanced Land Observing Satellite-2 (ALOS-2) is an Earth observation satellite, which was launched by the Japan Aerospace Agency in 2014. It is equipped with a phased array type L-band synthetic aperture radar (PALSAR-2) sensor and two optical cameras. Data obtained by ALOS-2 have been used for geohazard monitoring, deforestation monitoring, and sea ice observation [54].

The PALSAR-2 emits signal according to the selected mode with both horizontal (H) and vertical (V) polarization, and each of the scattering elements (i.e., HH, HV, VH, and VV) has a different sensitivity to different features of the ground surface, which helps to identify different land types [22]. The PALSAR-2 data used in this study were collected on 23 April 2015. In the ascending orbit, the angle of incidence is 30.4°, and the four polarization methods include the HH, VV, HV, and VH, as shown in Table 1.

Table 1. The main parameters of the fully polarimetric PALSAR-2 data.

Parameter Type	Data
Data Acquisition Date	23 April 2015
Polarization	HH, HV, VH, VV
Projection method	UTM
Incident angle	30.4°
Frequency	L-band (1.2 GHz)
Observation mode	Strip map (High-sensitive Quad)
Operation mode	SM2
Orbit path, frame	158, 730
Nominal resolution	5.1 × 4.3 m (Range × Azimuth)
Swath	40~50 km × 70 km (Range × Azimuth)
Processing Level	Level 1.1
File format	CEOS SAR
Observation and orbit direction	Right, Ascending

The PALSAR-2 data in the CEOS mode at the level of 1.1 in the study area were preprocessed by SNAP 7.0 software. The SAR data processing steps included: (1) generating a single look complex (SLC) image; (2) radiometric calibration; (3) multi looking (the oblique range directional vision was four, and the azimuthal vision was one) average the power of neighboring pixels [31]; (4) speckle filtering, using the refined Lee filter with the window size of 7 × 7, and removal of coherent noise; (5) terrain correction, correction of SAR geometric distortion using digital elevation model (DEM). The projection was based on the World Geodetic System Datum 1984 (WGS84) regarding the Universal Transverse Mercator (UTM) coordinate system at 44 degrees north latitude; (6) data resampling, image resizing to achieve an optimal resolution of 20 m × 20 m; (7) spatial subset, subset out the study area and typical land type in the experimental area. The preprocessing process of the PALSAR-2 data is shown in Figure 2.

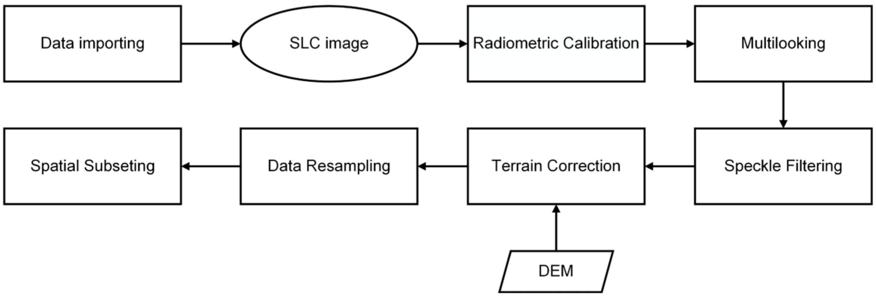

Figure 2. The preprocessing flowchart of the PALSAR-2 data.

2.2.2. Field Data

The fieldwork was conducted from 22 April 2015 to 7 May 2015. A total of 20 sites were selected for soil sampling based on visual observations of the land cover conditions and salinity, ensuring that sampling sites covered different land cover and soil characteristics, as shown in Figure 3.

Heavily salinized soil Heavily salinized soil Heavily salinized soil Desert

Moderately salinized soil Moderately salinized soil Moderately salinized soil Keriya River

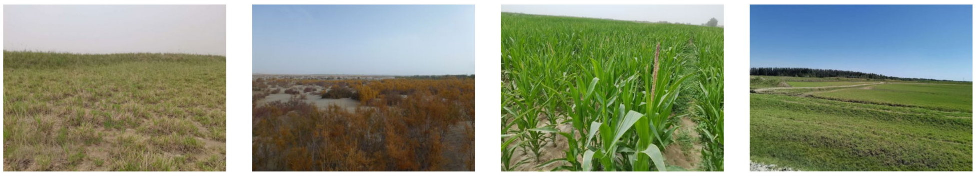

Slightly salinized soil Slightly salinized soil Agricultural land Grassland

Figure 3. Different degrees of salinized soil types of Keriya Oasis in the study area.

Soil sampling was conducted on the soil surface (0–10 cm), and the soils' physical and chemical characteristics such as soil salinity were measured in the laboratory. Soil samples were air-dried and sieved through 1-mm sieves, and the soil sample was mixed in a flask with distilled water at a ratio of 1:5. The flask was shaken manually for 3 min to allow the soil to infiltrate fully, and the fully-mixed solution was left to stand for 30 min. When the solution became clear, the solution was filtered and the total soluble salts were measured. In a certain concentration range, the salt content of the soil solution is positively correlated with the electrical conductivity, the more salt dissolved, the larger the EC, so the soil salt content can be measured indirectly based on the magnitude of the EC [55]. EC measurement is the most common characteristic used to determine soil salinity [56,57]. Therefore, many researchers use EC directly to determine and express soil salinity [58–60]. In this process, the electrical conductivity of the soil water was measured and expressed in ms/cm, and the total soluble salt content (expressed in g/kg) was calculated by the regression equation of EC and the total soluble salt. Different degrees of salinization (i.e., highly, moderately, and slightly saline soils) were determined based on the surface soil salt concentration, groundwater table, and vegetation coverage, as shown in Table 2.

Table 2. Soil salinity grading.

Symbol	Salinization Level	Characteristics
NS	Non-saline soil	EC value 0–2 (dsm^{-1}), no salt crusts or salt spots on the soil surface, crops can grow normally
SS	Slightly salinized soil	EC value 2–4 (dsm^{-1}), clear salt patches and salt crusts on the surface, the salt crust is thin (0~2 cm or so), high vegetation cover, at around 30%, groundwater level 1.4~3 m
MS	Moderately salinized soil	EC value 4–8 (dsm^{-1}), more salt crusts or salt spots on the soil surface, salt crust is 1~4 cm, vegetation cover of approximately 5~15%, groundwater level 1~2 m
HS	Heavily salinized soil	EC value 4–8 (dsm^{-1}), thick salt crust, and numerous salt patches on the soil surface, salt crust is 2~10 cm, vegetation covers less than 5%, groundwater level 0.5~1.5 m

3. Methodology

In this study, the polarization feature components obtained by different polarization decomposition methods were combined with two-dimensional feature space theory. The polarization characteristic components were analyzed to construct a quantitative inversion model of soil salinization. The overall workflow of the conducted research of the model construction process is presented in Figure 4.

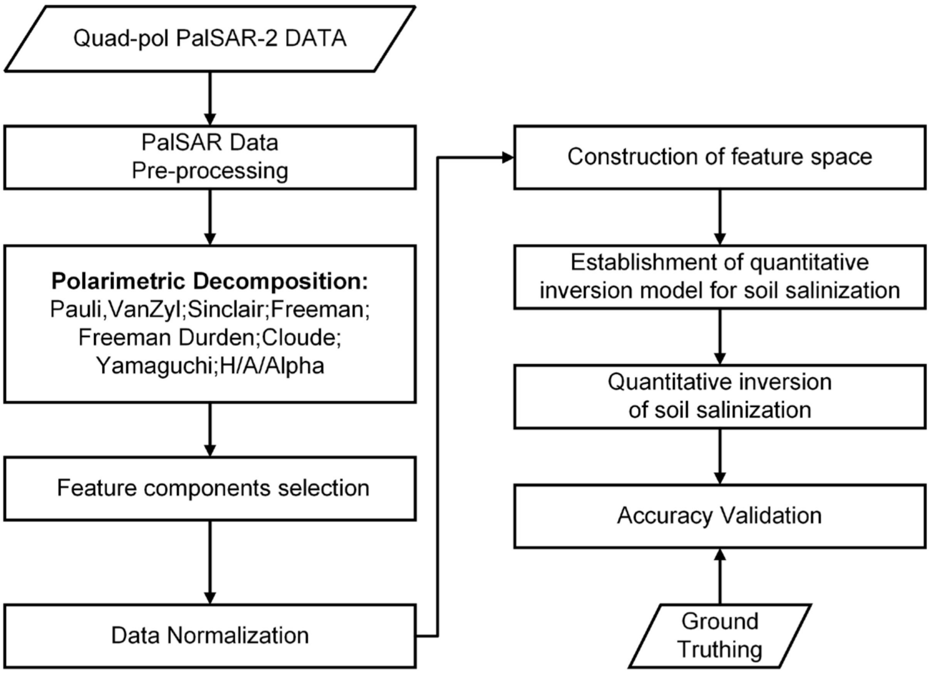

Figure 4. The overall workflow of the study.

3.1. Polarimetric Decomposition

The theorem of target polarization decomposition was first proposed by Huynen [61] in 1970, and after nearly 50 years of development, various polarization decomposition methods have emerged one after another [62]. It is a practical method used to analyze the ground target scattering mechanism embedded in SAR data by performing polarization decomposition and to fully explore the information hidden in the characteristic components of radar polarization decomposition [36,37].

Pauli decomposition is a common method of polarization decomposition [63]. Cloude initiated the Pauli decomposition in 1986 [64]. The Pauli decomposition takes four perfect orthogonal Pauli bases ($[S_a]$, $[S_b]$, $[S_c]$, $[S_d]$) as fundamental matrices, under the horizontal and vertical orthogonal bases (H, V), and the components of the Pauli bases are represented by the following 2 × 2 matrices

$$[S_a]=\frac{\begin{bmatrix}1&0\\0&1\end{bmatrix}}{\sqrt{2}},\ [S_b]=\frac{\begin{bmatrix}1&0\\0&-1\end{bmatrix}}{\sqrt{2}},\ [S_c]=\frac{\begin{bmatrix}0&1\\1&0\end{bmatrix}}{\sqrt{2}},\ [S_d]=\frac{\begin{bmatrix}0&-i\\i&0\end{bmatrix}}{\sqrt{2}} \tag{1}$$

The relationship between the components of the Pauli group and scattering types is shown in Table 3.

The scattering matrix $[S]$ for the target can be rewritten in the following form [22,65]

$$[S]=\begin{bmatrix}S_{hh}&S_{hv}\\S_{vh}&S_{vv}\end{bmatrix}=a\,[S_a]+b\,[S_b]+c\,[S_c]+d\,[S_d] \tag{2}$$

where S_{vh} and S_{hv} denote the cross-polarization components; S_{vv} and S_{hh} are the co-polarization components; a, b, c, and d represent complex coefficients of each component and can be expressed in the form of vector K

$$\text{K} = [a\ b\ c\ d] = \frac{((S_{hh} + S_{vv})\ (S_{hh} - S_{vv})\ (S_{hv} + S_{vh})\ \ i(S_{vh} - S_{hv}))^T}{\sqrt{2}} \tag{3}$$

where the superscript T indicates the matrix transpose.

When the scattering matrix satisfies the symmetry condition, i.e., reciprocity theorem ($S_{hv} = S_{vh}$), Equation (3) can be transformed into the following form

$$\text{K} = [a\ b\ c] = \frac{(S_{hh} + S_{vv}\ \ S_{hh} - S_{vv}\ \ \ 2S_{hv})^T}{\sqrt{2}} \tag{4}$$

Then, the polarization scattering matrix $[S]$ of the total power span can be expressed as follows [17]:

$$\text{Span} \ = \ |S_{hh}|^2 \ + |S_{hv}|_2 \ + |S_{vh}|_2 \ + |S_{vv}|_2 \ = \ |a|^2 + |b|^2 + |c|^2 + |d|^2 \tag{5}$$

where $|a|^2$, $|b|^2$, and $|c|^2$ correspond to distinct physical mechanisms.

Therefore, using Pauli decomposition coefficients, RGB images can be synthesized as follows

$$|a|^2 \ \rightarrow \ \text{Blue} \tag{6}$$

$$|b|^2 \ \rightarrow \ \text{Red} \tag{7}$$

$$|c|^2 \ \rightarrow \ \text{Green} \tag{8}$$

One of the advantages of the Pauli decomposition is its simplicity, and since the Pauli group is a perfect orthogonal group, the decomposition method has a relatively good suppression of noise. Therefore, Pauli decomposition has been widely used for PolSAR imagery [63].

Table 3. Physical interpretation of the Pauli decomposition in the horizontal–vertical orthogonal basis.

Pauli Matrix	Scattering Type	Physical Interpretation
$\begin{bmatrix} 1 & 0 \\ 0 & 1 \end{bmatrix}$	Odd scattering	Planar, spherical, and angular reflectors
$\begin{bmatrix} 1 & 0 \\ 0 & -1 \end{bmatrix}$	Even scattering	Two-sided angle
$\begin{bmatrix} 0 & 1 \\ 1 & 0 \end{bmatrix}$	$\frac{\pi}{4}$ even-order scattering	Two-sided angle with an inclination of $\frac{\pi}{4}$
$\begin{bmatrix} 0 & -i \\ i & 0 \end{bmatrix}$	Cross-polarization	No corresponding scattering mechanism exists

In addition, to exploit PALSAR-2 data better and to take full advantage of the polarization feature information of these data, several polarimetric decompositions have been proposed, and the corresponding polarization information has been obtained. The commonly used polarization decomposition methods include Cloude [66], Freeman [67], Freeman Durden [68], VanZyl [69], Yamaguchi [70], Sinclair [71], and H/A/Alpha [72] methods. The Cloude, Freeman, Freeman Durden, VanZyl, Yamaguchi, Sinclair, and H/A/Alpha polarization decomposition methods were applied to this study.

3.2. Feature Selection from ALOS-2 Polarimetric Imagery

Although multidimensional features can be extracted from PALSAR-2 data [73], there may be correlation and redundancy between these features, and some features can even be full of “noise” [74]. For quantitative inversion of salinization, images composed of multiple polarization feature components might not represent the salinization characteristics accurately, which could result in the unsatisfactory extraction of salinization information. In such a case, it is necessary to select the polarization feature component that can effectively and accurately invert salinization among multiple polarization feature components, i.e., it is necessary to conduct feature component selection.

The selection of polarization feature components in this study was mainly considered from three aspects, as follows. (1) SAR images are easily geometrically distorted and cannot be easily interpreted visually. Optical images are more reliable and easier to be interpreted than SAR images; additionally, more previous studies using optical images of the Keriya Oasis are available as references, and OvitalMap could provide a high-resolution interactive platform capable of providing images with maximum resolution of 1 × 1 m. Therefore, Landsat 8 OLI (30 × 30 m) (Figure 1e) and OvitalMap (https://www.ovital.com/, accessed on 28 September 2021) were used as reference images, and polarization feature components’ Signal-to-Noise Ratio (SNR) was calculated. The higher the SNR was, the clearer the image and the better the image quality and denoising effect were [75]. First, components with an SNR of less than 60 dB were eliminated; then, the polarization component with the largest SNR and smallest speckle noise among the three feature components of the same polarization decomposition was selected to reflect the target feature information better. The SNR values of the feature components are given in Table 4. (2) Meanwhile, 25 components were extracted from eight polarization decomposition methods; 300 groups of two-dimensional feature spaces were established, and three groups of them, consisting of six feature components with typical representation and regularity that could distinguish different degrees of salinized soils, were selected. (3) The energy information received by the SAR system reflected the scattering characteristics of the ground feature [45]. The Freeman, Pauli, Freeman Durden, Yamaguchi, VanZyl, Sinclair, and H/A/Alpha methods were used to calculate surface, volume, and double scattering values [17]. The polarization characteristic component was dominated by double scattering even in urban areas [31]. The surface scattering was mainly municipal surface backscattering information, which excluded the influence of vegetation [46]; the vegetation area was dominated by volume scattering [31]. Since information on the change in the land surface vegetation in the arid zone can better reflect the regional salinization status [76], the scattering-type characteristic component was broken down by gathering polarization, and the scattering type was selected as a component of volume scattering. The overall workflow of the feature selection process is presented in Figure 5.

Combining the above three aspects, four representative feature components were selected: Freeman_vol_g, Sinclair_g, Freeman Durden vol_g, and VanZyl_vol_g.

Table 4. The SNR values of the feature components (dB).

	Cloude	Freeman	Freeman Durden	Pauli	Sinclair	VanZyl	Yamaguchi	H/A/Alpha
Surface_b	356.067	308.391	252.007	225.301	203.320	240.865	268.901	21.0420
Volume_g	28.8860	412.218	378.320	213.868	225.270	373.967	268.092	21.0813
Double_b	72.6462	248.521	332.305	221.481	217.883	260.327	329.654	35.5327

3.3. Data Normalization

As there were significant differences between the individual parameters, data standardization was carried out to eliminate these differences.

The maximum and minimum values of the Freeman_vol_g (Fm_vol_g), Sinclair _g (Sin_ g), Freeman Durden_vol_g (FD_vol_g), VanZyl _vol_g (VZ_vol_g) were determined and then used to normalize the data as follows [16]

$$F = (\mathrm{Fm\_vol\_g} - \mathrm{Fm\_vol\_g}_{\min})/(\mathrm{Fm\_vol\_g}_{\max} - \mathrm{Fm\_vol\_g}_{\min}) \quad (9)$$

$$S = (\mathrm{Sin\ \_g} - \mathrm{Sin\ \_g}_{\min})/(\mathrm{Sin\ \_g}_{\max} - \mathrm{Sin\ \_g}_{\min}) \quad (10)$$

$$FD = (FD\_vol\_g - FD\_vol\_g_{min})/(FD\_vol\_g_{max} - FD\_vol\_g_{min}) \tag{11}$$

$$V = (VZ\_vol\_g - VZ\_vol\_g_{min})/(VZ\_vol\_g_{max} - VZ\_vol\_g_{min}) \tag{12}$$

where F, S, FD, V denotes the feature component value after data normalization.

Figure 5. The overall workflow of the feature selection process.

3.4. Feature Space

In recent studies, the feature space theory has been applied to many fields, including salinity monitoring, soil moisture inversion, and drought monitoring [77,78]. The extraction and monitoring of salinity information through the construction of feature spaces using various indicators extracted from optical data has been an advanced method for remote sensing research on soil salinity monitoring [76].

In recent years, there have been many studies on soil salinity information extraction based on selecting appropriate indicators to construct a two-dimensional feature space. For instance, Yongnian Zeng [14] used surface emissivity and vegetation indices to construct the albedo–NDVI two-dimensional feature space to reflect the desertification process. Wang Fei et al. [79] defined the relationship between the normalized difference vegetation index (NDVI) and salinity index (SI) and proposed the NDVI–SI feature space concept. Ding et al. [80] extracted the modified soil adjusted vegetation index (MSAVI) from remote sensing images and the wetness index (WI) from remote sensing imagery and, based on the obtained results, constructed a two-dimensional MSAVI–WI feature space for greenery in arid zones. As mentioned above, there is great potential to apply two-dimensional feature space theory to the quantitative monitoring and analysis of salinized land using existing remote sensing technology to develop quantitative methods and indicators for remote sensing monitoring of salinization [79]. The above-mentioned studies have all been based on the feature space of optical remote sensing data.

However, modeling studies using two-dimensional radar feature space have still been relatively rare in China. Therefore, the following question arises: is it possible to use radar feature components in two-dimensional spatial information modeling? Perhaps radar feature components show some advantages in the quantitative study of soil salinization. This study takes this question as a starting point and aims to construct a remote sensing information extraction model of soil salinity from radar data in two-dimensional feature space theory.

4. Results

4.1. Polarimetric Decomposition of PolSAR Data

Cloude, Freeman, Freeman Durden, Pauli, Sinclair, VanZyl, H/A/Alpha, and Yamaguchi polarization decomposition methods were applied to the PALSAR-2 images of the study area. Finally, a total of 25 polarization features were obtained from the polarized SAR images, and their characteristics are given in Table 5. The polarization decomposition of the RGB (R:|HH-VV|, G:|HV|, B:|HH+VV|) standard composite image is shown in Figure 6.

Table 5. Polarimetric features extracted from the PALSAR-2 data.

Polarization Decomposition	Number of Parameters	Polarimetric Parameter
Cloude	3	Cloude_dbl_r, Cloude_vol_g, Cloude_surf_b
Freeman	3	Freeman_dbl_r, Freeman_vol_g, Freeman_surf_b
Freeman Durden	3	Freeman Durden_dbl_r, Freeman Durden_vol_g, Freeman Durden_surf_b
Pauli	3	Pauli_r, Pauli_g, Pauli_b
Sinclair	3	Sinclair_r, Sinclair_g, Sinclair_b
VanZyl	3	VanZyl_dbl_r, VanZyl_vol_g, VanZyl_surf_b
H/A/Alpha	3	Entropy, Anisotropy, alpha
Yamaguchi	4	Yamaguchi_dbl_r, Yamaguchi_vol_g, Yamaguchi_surf_b, Yamaguchi_hlx

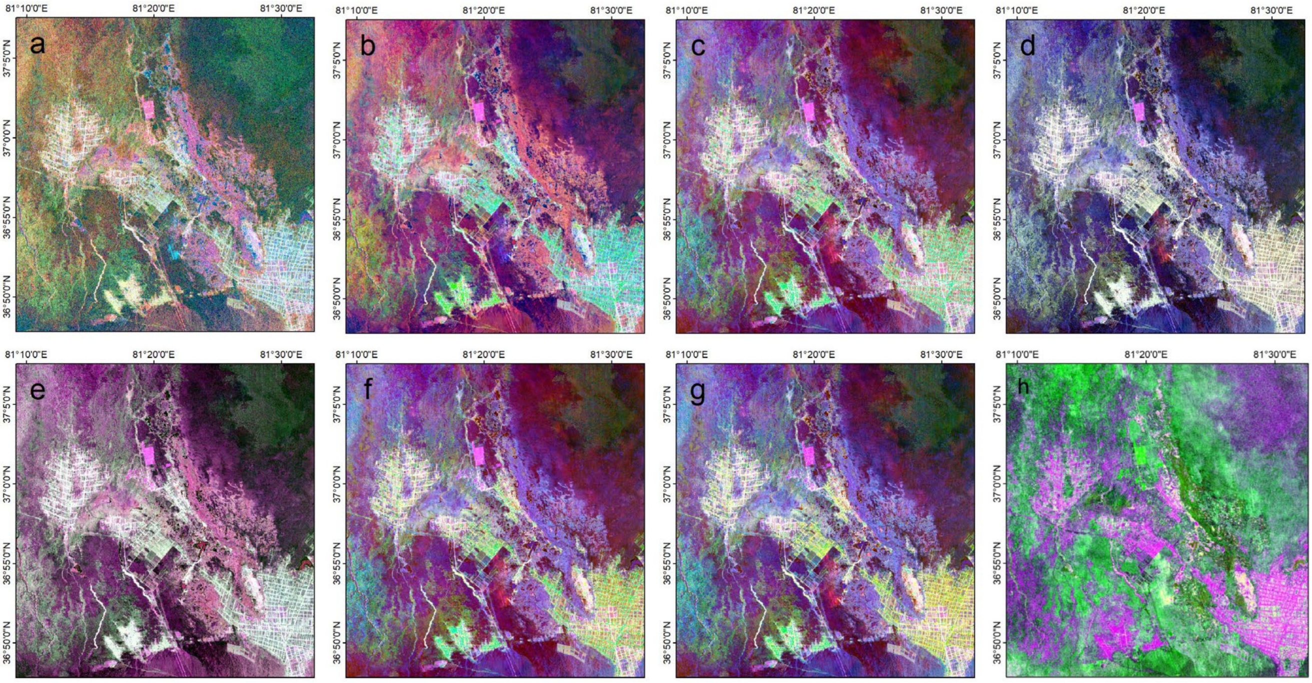

Figure 6. The polarization decomposition results of the RGB standard composite image obtained by: (**a**) Cloude; (**b**) Freeman; (**c**) Freeman Durden; (**d**) Pauli; (**e**) Sinclair; (**f**) VanZyl; (**g**) Yamaguchi; (**h**) H/A/Alpha decomposition methods.

4.2. Salinization Monitoring Models Based on Feature Spaces

4.2.1. Feature Space Construction

To determine different feature scattering types and their positions in different feature spaces and to analyze the distribution characteristics of soil salinity in the study area, an experimental area (Figure 1f) of typical land types was selected in the study area based on field survey data, and Landsat8 OLI and OvitalMap (https://www.ovital.com/, accessed on 28 September 2021) were used as reference images.

Using feature components, such as Freeman_vol_g, Sinclair_g, Freeman Durden vol_g, VanZyl_vol_g, the Sinclair_g–Freeman_vol_g (SF), VanZyl_vol_g–Freeman Durden_vol_g (VFD), and VanZyl_vol_g–Freeman vol_g (VF), three feature spaces were constructed.

As shown in Figures 7–9, the SF, VFD, and VF feature spaces had the same characteristics, i.e., there were obvious differences in the spatial distribution of different degrees of salinized soils in them. The blue areas of the scatter plot denote water bodies, and they are positioned mainly in the upper right part of the scatter plot, the green areas denote vegetation, the yellow areas represent slightly saline soils, the brown areas indicate moderately saline soils, and the red areas are heavily saline soils, and they are positioned mainly in the lower left part of the scatter plot. Figure 10 illustrates a simplified diagram of the three feature spaces.

4.2.2. Remote Sensing-Based Salinization Monitoring Model

Point A (1, 1) in Figure 10 was taken as the reference point (this point represents the "ideal point" with the best vegetation growth, the highest plant coverage, the highest surface humidity, and the lowest soil salinity). The distance from any point in the feature space to the reference point reflects the degree of salinization, therefore, the farther the distance is, the larger the salinization will be. For a point $C(C_1, C_2)$ in the SF, VFD, and VF feature spaces, the distance L from point C to point A can be calculated by

$$L = \sqrt{(1 - C_1)^2+(1 - C_2)^2} \tag{13}$$

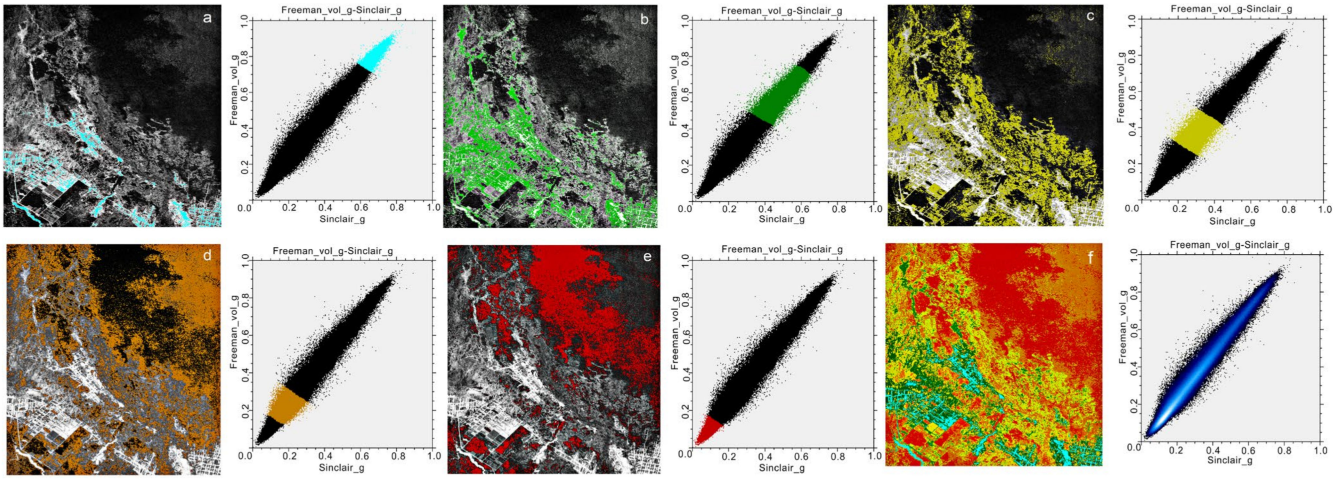

Figure 7. Illustration of different feature types and soil salinization contents in images in the SF feature space: (**a**) water bodies; (**b**) plant cover; (**c**) slight salinization; (**d**) moderate salinization; (**e**) severe salinization; (**f**) spatial distribution patterns of different levels of soil salinization.

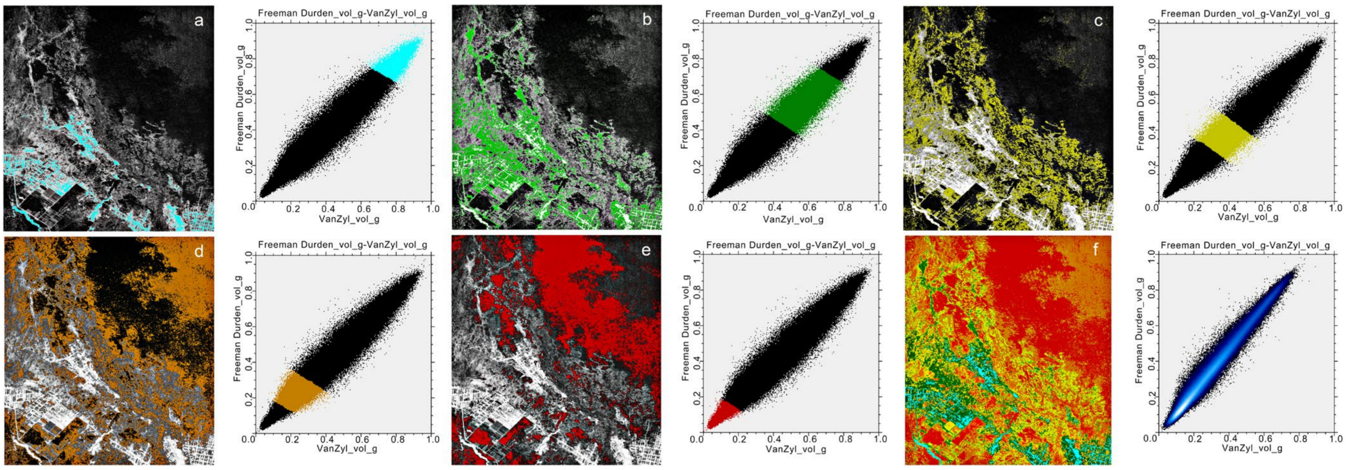

Figure 8. Illustration of different feature types and soil salinization contents in images in the VFD feature space: (**a**) water bodies; (**b**) plant cover; (**c**) slight salinization; (**d**) moderate salinization; (**e**) severe salinization; (**f**) spatial distribution patterns of different levels of soil salinization.

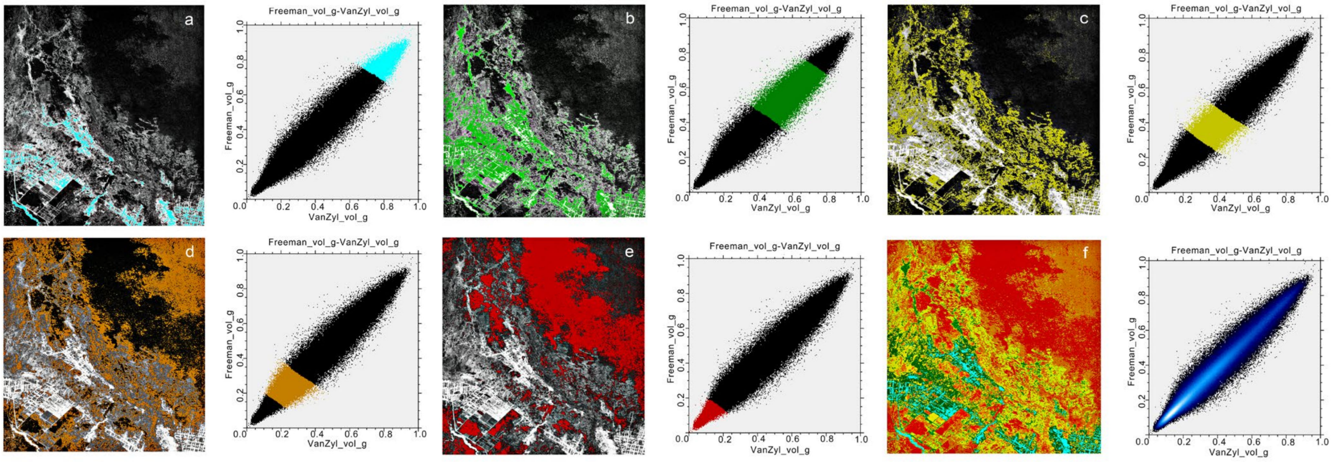

Figure 9. Illustration of different feature types and soil salinization contents in images in the VF feature space: (**a**) water bodies; (**b**) plant cover; (**c**) slight salinization; (**d**) moderate salinization; (**e**) severe salinization; (**f**) spatial distribution patterns of different levels of soil salinization.

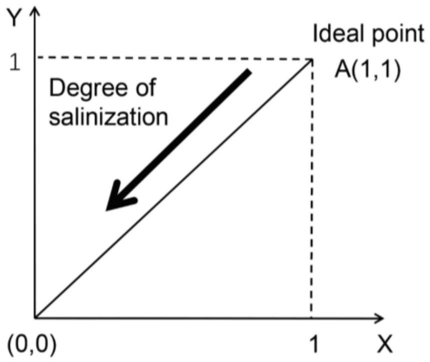

Figure 10. Simplified diagram of the feature space.

Then, three radar salinity monitoring models (Radar Salinity Detection Index—RSDI) were built using the following expressions

$$\text{RSDI1} = \sqrt{(1 - \text{Sinclair\_g})^2 + (1 - \text{Freeman\_vol\_g})^2} \tag{14}$$

$$\text{RSDI2} = \sqrt{(1 - \text{VanZyl\_vol\_g})^2 + (1 - \text{Freeman Durden\_vol\_g})^2} \tag{15}$$

$$\text{RSDI3} = \sqrt{(1 - \text{VanZyl\_vol\_g})^2 + (1 - \text{Freeman vol\_g})^2} \tag{16}$$

Using Equations (14)–(16), soil salinization inversions were conducted on the whole research area, as shown in Figure 11. In Figure 11, the darker the area is, the lower the degree of soil salinity is, and the brighter the area is, the higher the degree of soil salinity is. The darker areas were mainly in and around the oasis, while the brighter areas were in the lower terrain areas on the oasis periphery.

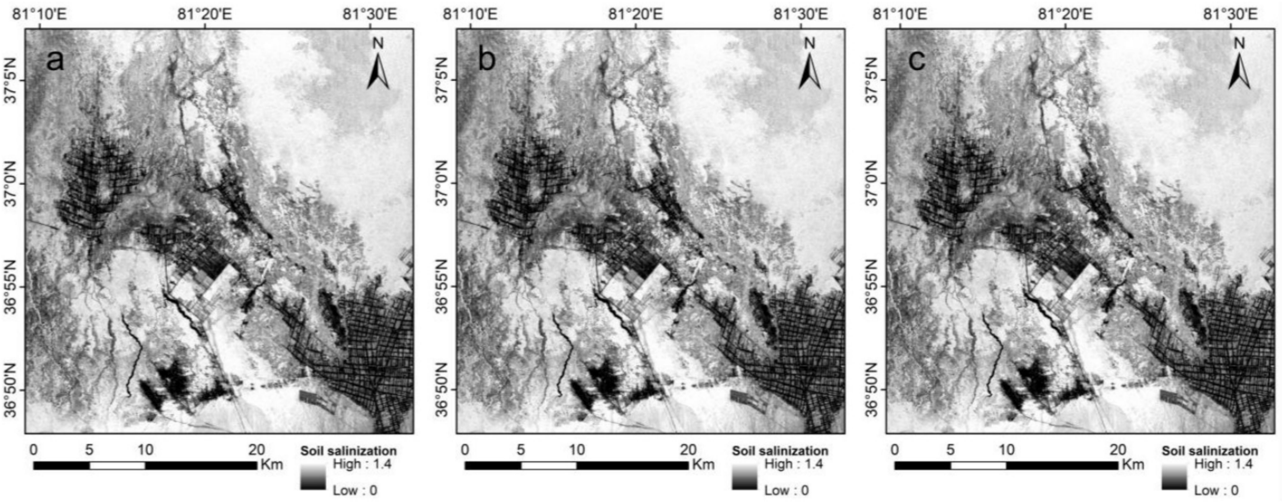

Figure 11. Spatial distribution patterns of different levels of soil salinization: (**a**) RSDI1; (**b**) RSDI2; (**c**) RSDI3.

To verify the sensitivity of the three soil salinity monitoring models, the saline soils correlation analysis was carried out using the salt content of 20 measured sample points on the surface. As shown in Figure 12, the inversion accuracy values of RSDI1, RSDI2, and RSDI3 were $R^2 = 0.63$, $R^2 = 0.61$, and $R^2 = 0.62$, respectively; thus, all three correlations exceed 0.5. However, the overall correlation was not high. Therefore, RSDI1 was selected as the best model for monitoring soil salinity in the Keriya Oasis among the three models.

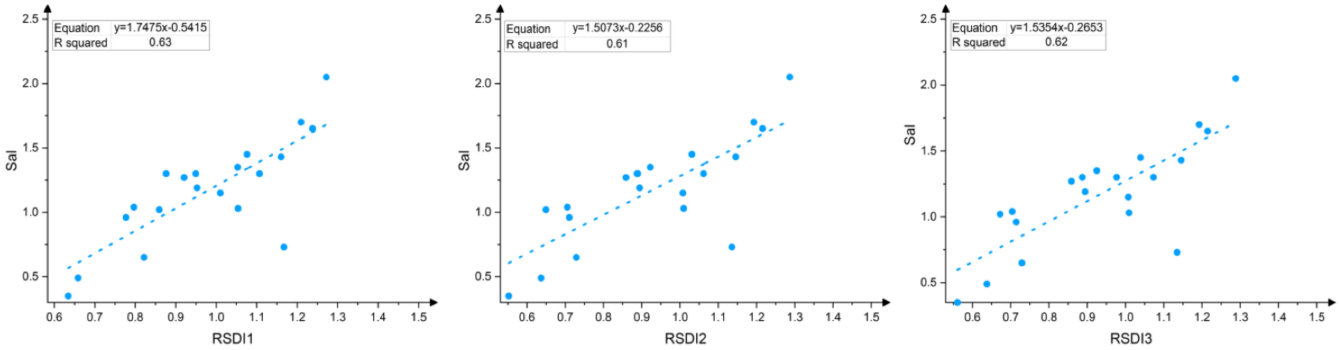

Figure 12. Accuracy comparison between the RSDI1, RSDI2, and RSDI3 models.

Using the RSDI models (RSDI1, RSDI2, and RSDI3), information on salinization in the Keriya Oasis was calculated. To distinguish different soil salinity levels better, Landsat 8 (Figure 1e) and OvitalMap were used as reference images. Additionally, based on the fieldwork and previous research [32,53], each salinity index was divided into three categories: a salinity index of $0.8 < \text{RSDI} < 1.0$ indicated slight salinization; a salinity index of $1 < \text{RSDI} < 1.2$ indicated moderate salinization; a salinity index of $1.2 < \text{RSDI} < 1.4$ indicated severe salinization. In addition, a salinity index of $0 < \text{RSDI} < 0.6$ denoted water bodies, and a salinity index of $0.5 < \text{RSDI} < 0.8$ denoted plant cover. The distribution of different degrees of soil salinization is presented in Figure 13.

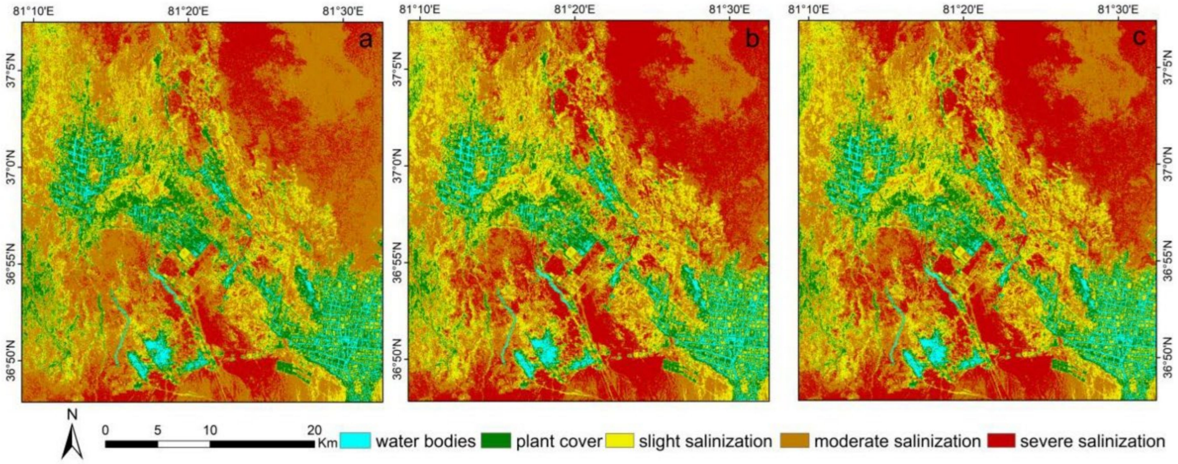

Figure 13. Spatial distribution patterns of different levels of soil salinization (**a**) RSDI1; (**b**) RSDI2; (**c**) RSDI3.

As shown in Figure 13, the areas of moderate and severe salinization were larger and mainly positioned in the southern and north-eastern regions; the range of mild salinization was relatively small and mainly distributed in the central region and near rivers and lakes. The overall salinization in the east was higher than the overall salinization in the west, and it appeared as a transition from mild to moderate salinization and then to severe salinization. The overall salinization trend was low to medium-high, which is consistent with the actual survey.

5. Discussion

Currently, polarization decomposition techniques have been commonly used to classify remote sensing images [17]. However, there has been little research on quantitative parameter retrieval using polarization decomposition techniques [81]. With the development of polarization decomposition techniques, polarization decomposition has been increasingly used in quantitative parameter retrieval [82]. In this study, based on the feature space theory combined with the radar remote sensing image analysis and field investigation, it was found that the soil salinization process is reflected in the middle of the feature constructed by the Freeman_vol_g, Sinclair_g, Freeman Durden vol_g, and VanZyl_vol_g. Based on the analysis results, the RSDI1, RSDI2, and RSDI3 soil salinization remote sensing monitoring models were constructed. The validation results show that the three soil salinity monitoring models provide an accurate indication of salinity degree in surface soils. Based on the results, the RSDI1 model is more sensitive to the salt content of the topsoil among all the models, and it is followed by the RSDI2 and RSDI3 models. Based on the inversion results in Figure 10, moderately and heavily saline land is mainly located in the north-eastern part of the study area. This is probably because the spatial and temporal distribution of soil salinity is strongly related to the cyclical processes of water resources. The movement of water and salt plays a key role in the process of soil salinization, the effects of salt and water are mutually restricted to each other, and the spatial distribution of soil moisture and salinity can be directly influenced by the flow of surface and groundwater [83]. Evaporation of water increases as the groundwater table rises, and more salts accumulate at the surface through capillary water. The limited precipitation and high evaporation in arid and semi-arid areas hinder the leaching process of salts to deep soils depths [83], namely, as salt moves with water and soil salinity is susceptible to shifts in the response to changes in moisture, soil salts from higher ground tend to accumulate at the lower ground due to the topography [76]. The topography of the Keriya Oasis is higher in the south than in the north, so the northern part of the Oasis is more saline than the southern part.

However, the overall correlation between the three model inversions was not high, and the reasons for this might be due to the following: (1) Underutilization of the polarization properties of the PolSAR data. (2) The effect of radar image speckle noise because although the radar images were filtered during the data preprocessing process, the speckle noise was not completely removed; (3) The polarization characteristic components used in this study belong to volume scattering components. It should be noted that the volume scattering components are sensitive to vegetation, so the reflection is strong in areas with vegetation but weak in areas with less or without vegetation. Accordingly, the soil salinization degree is relatively low in areas with more vegetation but relatively high in areas with less vegetation. However, the inversion accuracy of soil salinity was low, and there might be interference from other information, such as topography, soil composition, vegetation growth in different areas, vegetation type, vegetation height, and groundwater level. (4) There were many salt-tolerant plants in the area and vegetation coverage was not the lowest in regions with severe salinization, which could affect the inversion accuracy. (5) Only some of the polarization features of the PolSAR data were retained at the cost of inevitably losing part of the useful polarization information in terms of feature subset selection.

Many researchers have used different research methods for quantitative inversion of soil salinity and have achieved desirable results. Wang Fei et al. [79] proposed an NDVI–SI feature space by using Landsat-8 OLI data and constructed a salinization detection index (SDI) model, and the result showed that the soil surface salinity was highly correlated with SDI with R^2 = 0.8596. Feng Juan et al. [84] proposed the albedo–MSAVI feature space concept with Landsat-8 OLI to construct different index models for monitoring soil salinity, and the coefficient of determination of the model and soil salinity was 0.96, which can better reflect the salinity of the oasis. The feature space theory has been widely applied to remote sensing data, but mainly using optical remote sensing data, and fewer studies have applied radar images to construct feature space to invert the salinity of soils. Zaytungul et al. [53] took the soil salt content as the dependent variable, used the backscattering coefficient of four polarized PALSAR-2 data, soil water content, soil pH value, and measured values of soil salt, and established a quantitative inversion model by using a multiple linear regression model, geological weighted regression model, and BP neural network model. Yao Gao et al. [85] evaluated the effectiveness of the improved medium mixing model and integral equation model for describing saline soils. Finally, a linear regression model for salt content monitoring was developed. Although the above studies constructed soil salinity inversion models using radar images and achieved good results, there are fewer studies that apply the feature space theory to radar images to construct soil salinity inversion models.

In this study, radar feature space was established by using the theory of feature space, combined with the theory of polarization decomposition of radar images and field investigations, the monitoring model of soil salinity was constructed, and the inversion accuracy was relatively desirable. Although the results of this quantitative inversion model of soil salinity were somewhat satisfactory in this particular arid environment, the generalizability of the model in other areas needs further research and evaluation.

6. Conclusions

In this study, an investigation of the soil salinization in Keriya Oasis of Xinjiang, China, is conducted using the satellite-based PolSAR imagery. The advantages of polarization decomposition and feature space theory were fully utilized to invert salinized soils using quad-polarized PALSAR-2 images. Integrated multiple polarization decomposition methods (Cloude, Freeman, Freeman Durden, Pauli, Sinclair, VanZyl, Yamaguchi, and H/A/Alpha) were used to extract polarization parameters related to the physical scattering mechanism of soil salinity.

The main conclusions of our work are as follows: (1) the feature components of PALSAR-2 data in the study area were selected, consisting of four polarized feature components, including Freeman_vol_g, Sinclair_g, Freeman Durden vol_g, and VanZyl_vol_g; (2) Based on the selected feature components, the Sinclair_g–Freeman_vol_g, VanZyl_vol_g–Freeman Durden_vol_g, and VanZyl_vol_g–Freeman vol_g, three feature spaces were constructed, and the RSDI1, RSDI2, and RSDI3 soil salinity quantitative inversion models were also established. (3) Then, validation of the models used data of field-measured surface soil salinity. (4) The analysis and comparison results of typical feature spaces show that the RSDI1 model ($R^2 = 0.63$) has better applicability to the salinization monitoring in Keriya Oasis than models RSDI2 ($R^2 = 0.61$) and RSDI3 ($R^2 = 0.62$). The obtained results demonstrate the potential of feature space models in extracting salinization information using PolSAR data.

This study not only makes full use of the rich polarization information in PolSAR data but also takes advantage of the two-dimensional feature space with simple principles and convenient operation to construct a quantitative inversion model that can effectively and quickly extract regional soil salinity information, providing a new perspective for future soil salinity monitoring.

Author Contributions: Conceptualization, N.M. and I.N.; methodology, N.M. and I.N.; software, N.M. and A.A.; validation, N.M. and I.N.; formal analysis, N.M. and I.N.; investigation, I.N., N.M., A.A., S.X. and J.Z.; data curation, N.M., A.A. and S.X.; writing—original draft preparation, N.M.; writing—review and editing, I.N.; supervision, I.N.; project administration, I.N.; funding acquisition, I.N. All authors have read and agreed to the published version of the manuscript.

Funding: This research was sponsored by National Natural Science Foundation of China [No. 42061065, No. U1703237 and No. 41561089].

Data Availability Statement: Not applicable.

Acknowledgments: The authors gratefully acknowledge I.N. who participated in the design of the study, provided theoretical and technical guidance, and suggested modifications; also, A.A., S.X. and J.Z. for their comments on data processing and paper writing. Finally, we also extend our hearty gratitude to the anonymous reviewers of this manuscript for their constructive comments and helpful suggestions, which strengthened the manuscript.

Conflicts of Interest: The authors declare no conflict of interest.

References

1. Zhang, X.G.; Huang, B. Prediction of soil salinity with soil-reflected spectra: A comparison of two regression methods. *Sci. Rep.* **2019**, *9*, 8. [CrossRef] [PubMed]
2. Dong, F.; Tang, Y.J.; Xing, X.R.; Liu, Z.H.; Xing, L.T. Formation and Evolution of Soil Salinization in Shouguang City Based on PMS and OLI/TM Sensors. *Water* **2019**, *11*, 15. [CrossRef]
3. Libutti, A.; Cammerino, A.R.B.; Monteleone, M. Risk Assessment of Soil Salinization Due to Tomato Cultivation in Mediterranean Climate Conditions. *Water* **2018**, *10*, 19. [CrossRef]
4. Rengasamy, P. World salinization with emphasis on Australia. *J. Exp. Bot.* **2006**, *57*, 1017–1023. [CrossRef]
5. Singh, A. Soil salinization management for sustainable development: A review. *J. Environ. Manag.* **2021**, *277*, 111383. [CrossRef]
6. Pennock, D.; McKenzie, N.; Montanarella, L. *Status of the World's Soil Resources*; Technical Summary; FAO: Rome, Italy, 2015.
7. Nachshon, U. Cropland soil salinization and associated hydrology: Trends, processes and examples. *Water* **2018**, *10*, 1030.
8. Jamil, A.; Riaz, S.; Ashraf, M.; Foolad, M. Gene expression profiling of plants under salt stress. *Crit. Rev. Plant. Sci.* **2011**, *30*, 435–458. [CrossRef]
9. Zhang, J.; Jiang, J.; Shan, Q.; Chen, G.; Wang, Y.; Shen, L.; Pan, C.; Wu, H.; Abarquez, A. Soil salinization and ecological remediation by planting trees in China. In Proceedings of the 2010 International Conference on Mechanic Automation and Control Engineering, Wuhan, China, 26–28 June 2010; IEEE: Piscataway, NJ, USA, 2010; pp. 1349–1352.
10. Ivushkin, K.; Bartholomeus, H.; Bregt, A.K.; Pulatov, A.; Kempen, B.; de Sousa, L. Global mapping of soil salinity change. *Remote Sens. Environ.* **2019**, *231*, 12. [CrossRef]
11. Ding, J.; Yang, S.; Shi, Q.; Wei, Y.; Wang, F. Using Apparent Electrical Conductivity as Indicator for Investigating Potential Spatial Variation of Soil Salinity across Seven Oases along Tarim River in Southern Xinjiang, China. *Remote Sens.* **2020**, *12*, 2601. [CrossRef]
12. Tian, C.; Mai, W.; Zhao, Z. Study on key technologies of ecological management of saline alkali land in arid area of Xinjiang. *Acta Ecol. Sin.* **2016**, *3636*, 7064–7068.
13. Guo, B.; Zang, W.Q.; Zhang, R. Soil Salizanation Information in the Yellow River Delta Based on Feature Surface Models Using Landsat 8 OLI Data. *IEEE Access* **2020**, *8*, 94394–94403. [CrossRef]
14. Guo, B.; Zang, W.Q.; Luo, W.; Wen, Y.; Yang, F.; Han, B.M.; Fan, Y.W.; Chen, X.; Qi, Z.; Wang, Z.; et al. Detection model of soil salinization information in the Yellow River Delta based on feature space models with typical surface parameters derived from Landsat8 OLI image. *Geomat. Nat. Hazards Risk* **2020**, *11*, 288–300. [CrossRef]
15. Ren, D.Y.; Wei, B.Y.; Xu, X.; Engel, B.; Li, G.Y.; Huang, Q.Z.; Xiong, Y.W.; Huang, G.H. Analyzing spatiotemporal characteristics of soil salinity in arid irrigated agro-ecosystems using integrated approaches. *Geoderma* **2019**, *356*, 12. [CrossRef]
16. Zeng, Y.; Xiang, N.; Feng, Z. Albedo-NDVI space and remote sensing synthesis index models for desertification monitoring. *Sci. Geogr. Sin.* **2006**, *26*, 75. [CrossRef]
17. Xie, Q.; Meng, Q.; Zhang, L.; Wang, C.; Sun, Y.; Sun, Z. A Soil Moisture Retrieval Method Based on Typical Polarization Decomposition Techniques for a Maize Field from Full-Polarization Radarsat-2 Data. *Remote Sens.* **2017**, *9*, 168. [CrossRef]
18. Ma, G.; Ding, J.; Han, L.; Zhang, Z.; Ran, S. Digital mapping of soil salinization based on Sentinel-1 and Sentinel-2 data combined with machine learning algorithms. *Reg. Sustain.* **2021**, *2*, 177–188. [CrossRef]
19. Metternicht, G.I.; Zinck, J.A. Remote sensing of soil salinity: Potentials and constraints. *Remote Sens. Environ.* **2003**, *85*, 1–20. [CrossRef]
20. Allbed, A.; Kumar, L. Soil Salinity Mapping and Monitoring in Arid and Semi-Arid Regions Using Remote Sensing Technology: A Review. *Adv. Remote Sens.* **2013**, *2*, 373–385. [CrossRef]
21. Wang, J.Q.; Peng, J.; Li, H.Y.; Yin, C.Y.; Liu, W.Y.; Wang, T.W.; Zhang, H.P. Soil Salinity Mapping Using Machine Learning Algorithms with the Sentinel-2 MSI in Arid Areas, China. *Remote Sens.* **2021**, *13*, 14. [CrossRef]
22. Qi, Z.X.; Yeh, A.G.O.; Li, X.; Lin, Z. A novel algorithm for land use and land cover classification using RADARSAT-2 polarimetric SAR data. *Remote Sens. Environ.* **2012**, *118*, 21–39. [CrossRef]
23. Periasamy, S.; Ravi, K.P. A novel approach to quantify soil salinity by simulating the dielectric loss of SAR in three-dimensional density space. *Remote Sens. Environ.* **2020**, *251*, 17. [CrossRef]
24. Rhoades, J.D.; Chanduvi, F.; Lesch, S. *Soil Salinity Assessment: Methods and Interpretation of Electrical Conductivity Measurements*; The Governments of Europe: Rome, Italy, 1999; Volume 57.
25. Bell, D.; Menges, C.; Ahmad, W.; van Zyl, J.J. The application of dielectric retrieval algorithms for mapping soil salinity in a tropical coastal environment using airborne polarimetric SAR. *Remote Sens. Environ.* **2001**, *75*, 375–384. [CrossRef]
26. Lasne, Y.; Paillou, P.; Freeman, A.; Farr, T.; McDonald, K.C.; Ruffie, G.; Malezieux, J.-M.; Chapman, B.; Demontoux, F. Effect of salinity on the dielectric properties of geological materials: Implication for soil moisture detection by means of radar remote sensing. *IEEE Trans. Geosci. Remote Sens.* **2008**, *46*, 1674–1688. [CrossRef]
27. Grissa, M.; Abdelfattah, R.; Mercier, G.; Zribi, M.; Chahbi, A.; Lili-Chabaane, Z. Empirical model for soil salinity mapping from SAR data. In Proceedings of the Geoscience & Remote Sensing Symposium, Vancouver, BC, Canada, 24–29 July 2011.
28. Taghadosi, M.M.; Hasanlou, M.; Eftekhari, K. Soil salinity mapping using dual-polarized SAR Sentinel-1 imagery. *Int. J. Remote Sens.* **2019**, *40*, 237–252. [CrossRef]
29. Gong, H.Z.; Shao, Y.; Brisco, B.; Hu, Q.R.; Tian, W. Modeling the dielectric behavior of saline soil at microwave frequencies. *Can. J. Remote Sens.* **2013**, *39*, 17–26. [CrossRef]

30. Singh, A.; Meena, G.K.; Kumar, S.; Gaurav, K. Evaluation of the Penetration Depth of L-and S-Band (NISAR mission) Microwave SAR Signals into Ground. In Proceedings of the 2019 URSI Asia-Pacific Radio Science Conference (AP-RASC), New Delhi, India, 9–15 March 2019; IEEE: Piscataway, NJ, USA, 2019; p. 1.
31. Jakob Van Zyl, Y.K. *Synthetic Aperture Radar Polarimetry*; John Wiley & Sons: Hoboken, NJ, USA, 2011; Volume 2.
32. Nurmemet, I.; Sagan, V.; Ding, J.L.; Halik, U.; Abliz, A.; Yakup, Z. A WFS-SVM Model for Soil Salinity Mapping in Keriya Oasis, Northwestern China Using Polarimetric Decomposition and Fully PolSAR Data. *Remote Sens.* **2018**, *10*, 20. [CrossRef]
33. Boerner, W.M. Recent advances in extra-wide-band polarimetry, interferometry and polarimetric interferometry in synthetic aperture remote sensing and its applications. *IEEE Proc. Radar Sonar Navig.* **2003**, *150*, 113–124. [CrossRef]
34. Yang, J.; Yamaguchi, Y.; Lee, J.S.; Touzi, R.; Boerner, W.M. Applications of Polarimetric SAR. *J. Sens.* **2015**, *2015*, 316391. [CrossRef]
35. Xu, M. Extraction and Geometrical Structure Retrieval of Man-made Target in POLSAR Imagery. Ph.D. Thesis, Engineering-National University of Defense Technology, Changsha, China, 2008.
36. Trudel, M.; Magagi, R.; Granberg, H.B. Application of Target Decomposition Theorems Over Snow-Covered Forested Areas. *IEEE Trans. Geosci. Remote Sens.* **2009**, *47*, 508–512. [CrossRef]
37. Touzi, R. Target scattering decomposition in terms of roll-invariant target parameters. *IEEE Trans. Geosci. Remote Sens.* **2007**, *45*, 73–84. [CrossRef]
38. Hoekman, D.H.; Quinones, M.J. Land cover type and biomass classification using AirSAR data for evaluation of monitoring scenarios in the Colombian Amazon. *IEEE Trans. Geosci. Remote Sens.* **2000**, *38*, 685–696. [CrossRef]
39. Schuler, D.L.; Lee, J.S. Mapping ocean surface features using biogenic slick-fields and SAR polarimetric decomposition techniques. *IEEE Proc. Radar Sonar Navig.* **2006**, *153*, 260–270. [CrossRef]
40. Gama, F.F.; Santos, J.D.; Mura, J.C. Eucalyptus Biomass and Volume Estimation Using Interferometric and Polarimetric SAR Data. *Remote Sens.* **2010**, *2*, 939–956. [CrossRef]
41. Souyris, J.C.; Henry, C.; Adragna, F. On the use of complex SAR image spectral analysis for target detection: Assessment of polarimetry. *IEEE Trans. Geosci. Remote Sens.* **2003**, *41*, 2725–2734. [CrossRef]
42. Li, J.; Huang, P.; Wang, X.; Pan, X. Image edge detection based on beamlet transform. *J. Syst. Eng. Electron.* **2009**, *20*, 1–5. [CrossRef]
43. Cui, Y.; Yang, J.; Zhang, X.Z. New CFAR target detector for SAR images based on kernel density estimation and mean square error distance. *J. Syst. Eng. Electron.* **2012**, *23*, 40–46. [CrossRef]
44. Lee, J.S.; Grunes, M.R.; Ainsworth, T.L.; Du, L.J.; Schuler, D.L.; Cloude, S.R. Unsupervised classification using polarimetric decomposition and the complex Wishart classifier. *IEEE Trans. Geosci. Remote Sens.* **2002**, *37*, 2249–2258. [CrossRef]
45. Ersahin, K.; Cumming, I.G.; Ward, R.K. Segmentation and Classification of Polarimetric SAR Data Using Spectral Graph Partitioning. *IEEE Trans. Geosci. Remote Sens.* **2010**, *48*, 164–174. [CrossRef]
46. He, C.; Xia, G.; Sun, H. SAR images classification method based on Dempster-Shafer theory and kernel estimate. *J. Syst. Eng. Electron.* **2007**, *18*, 210–216. [CrossRef]
47. Lu, D.; Weng, Q. A survey of image classification methods and techniques for improving classification performance. *Int. J. Remote Sens.* **2007**, *28*, 823–870. [CrossRef]
48. Weilei, D. The Research on Target Recognition Methods based on Polarization Radar. Master's Thesis, Harbin Engineering University, Harbin, China, 2013.
49. Luo, C.; Feng, X.; Liu, C.; Zhang, Y.; Nilot, E.; Zhang, M.; Dong, Z.; Zhou, H. Full-polarimetric GPR for detecting ice fractures. In Proceedings of the 2018 17th International Conference on Ground Penetrating Radar (GPR), Rapperswil, Switzerland, 18–21 June 2018; IEEE: Piscataway, NJ, USA, 2018; pp. 1–4.
50. Isak, G.; Nurmemet, I.; Duan, S.S. The Extraction of Saline Soil Information in Typical Oasis of Arid Area Using Fully Polarimetric Radarsat-2 data. *China Rural Water Hydropower* **2018**, *12*, 13–19.
51. Seydehmet, J.; Lv, G.H.; Nurmemet, I.; Aishan, T.; Abliz, A.; Sawut, M.; Abliz, A.; Eziz, M. Model prediction of secondary soil salinization in the Keriya Oasis, Northwest China. *Sustainability* **2018**, *10*, 656. [CrossRef]
52. Mamat, Z.; Yimit, H.; Lv, Y. Spatial Distributing Pattern of Salinized Soils and their Salinity in Typical Area of Yutian Oasis. *Chin. J. Soil Sci.* **2013**, *44*, 1314–1320.
53. Yakup, Z.; Sawut, M.; Abdujappar, A.; Zhang, D. Soil salinity inversion in Yutian Oasis based on PALSAR radar data. *Resour. Sci.* **2018**, *40*, 2110–2117.
54. Yang, X. The oases along the Keriya River in the Taklamakan Desert, China, and their evolution since the end of the last glaciation. *Environ. Geol.* **2001**, *41*, 314–320. [CrossRef]
55. Wu, Y.; Wang, W.; Wang, H.; Zhang, Z. Analysis of variation of soil salt with new electric conductivity index. *Acta Pedol. Sin.* **2011**, *48*, 869–873.
56. McNeill, J.D. Rapid, accurate mapping of soil salinity by electromagnetic ground conductivity meters. *Adv. Meas. Soil Phys. Prop. Bring. Theory Pract.* **1992**, *30*, 209–229.
57. Rhoades, J. Electrical conductivity methods for measuring and mapping soil salinity. *Adv. Agron.* **1993**, *49*, 201–251.
58. Allbed, A.; Kumar, L.; Aldakheel, Y.Y. Assessing soil salinity using soil salinity and vegetation indices derived from IKONOS high-spatial resolution imageries: Applications in a date palm dominated region. *Geoderma* **2014**, *230*, 1–8. [CrossRef]
59. U.S. Salinity Laboratory Staff. *Determination of the Properties of Saline and Alkali Soils*; United State Department of Agriculture: Washington, DC, USA, 1954; pp. 7–33.

60. Abuelgasim, A.; Ammad, R. Mapping soil salinity in arid and semi-arid regions using Landsat 8 OLI satellite data. *Remote Sens. Appl. Soc. Environ.* **2019**, *13*, 415–425. [CrossRef]
61. Huynen, J.R. Phenomenological Theory of Radar Targets. Ph.D. Thesis, Technical University, Delft, The Netherlands, 1970.
62. An, W.; Yi, C.; Jian, Y. Three-Component Model-Based Decomposition for Polarimetric SAR Data. *IEEE Trans. Geosci. Remote Sens.* **2010**, *48*, 2732–2739. [CrossRef]
63. Cloude, S.R.; Pottier, E. A review of target decomposition theorems in radar polarimetry. *IEEE Trans. Geosci. Remote Sens.* **1996**, *34*, 498–518. [CrossRef]
64. Cloude, S.R. Group Theory and Polarisation Algebra. *Optik* **1986**, *75*, 26–36.
65. Haldar, D.; Das, A.; Mohan, S.; Pal, O.; Hooda, R.S.; Chakraborty, M. Assessment of L-Band SAR Data at Different Polarization Combinations for Crop and Other Landuse Classification. *Prog. Electromagn. Res. B* **2012**, *36*, 303–321. [CrossRef]
66. Cloude, S.R. Target decomposition theorems in radar scattering. *Electron. Lett.* **2007**, *21*, 22–24. [CrossRef]
67. Freeman, A. Fitting a Two-Component Scattering Model to Polarimetric SAR Data from Forests. *IEEE Trans. Geosci. Remote Sens.* **2007**, *45*, 2583–2592. [CrossRef]
68. Freeman, A.; Durden, S.L. A three-component scattering model for polarimetric SAR data. *IEEE Trans. Geosci. Remote Sens.* **1998**, *36*, 963–973. [CrossRef]
69. Vanzyl, J.J. Application of Cloude's target decomposition theorem to polarimetric imaging radar data. In *Radar Polarimetry; Proceedings of the SPIE'92, San Diego, CA, USA, 1992*; SPIE: Washington, DC, USA, 1993; pp. 184–191. [CrossRef]
70. Yamaguchi, Y.; Moriyama, T.; Ishido, M.; Yamada, H. Four-component scattering model for polarimetric SAR image decomposition. *Tech. Rep. Ieice Sane* **2005**, *104*, 1699–1706. [CrossRef]
71. Sinclair, G. The Transmission and Reception of Elliptically Polarized Waves. *Proc. Ire.* **1950**, *38*, 148–151. [CrossRef]
72. Cloude, S.R.; Pottier, E. An entropy based classification scheme for land applications of polarimetric SAR. *IEEE Trans. Geo Remote Sens.* **1997**, *35*, 68–78. [CrossRef]
73. Pottier, E.; Ferro-Famil, L. PolSARPro V5.0: An ESA educational toolbox used for self-education in the field of POLSAR and POL-INSAR data analysis. In Proceedings of the 2012 Geoscience and Remote Sensing Symposium (IGARSS), Munich, Germany, 22–27 July 2012; IEEE International: Piscataway, NJ, USA, 2012.
74. Sun, X.; Yang, X.L.; Shang-Tan, T.U.; Huang, P.P.; Yang, W. Unsupervised Classification of PolSAR Images by Combining Feature Selection and Large Scale Spectral Clustering. *J. Signal Process.* **2016**, *32*, 684.
75. Hong, C.; Na, L.; Xin Rui, W. *Introduction to Digital Media Technology*; Beijing University of Posts and Telecommunications Press: Beijing, China, 2015.
76. Ding, J.; Yao, Y.; Wang, F. Detecting soil salinization in arid regions using spectral feature space derived from remote sensing data. *Acta Ecol. Sin.* **2014**, *34*, 4620–4631. [CrossRef]
77. Guo, B.; Yang, F.; Fan, Y.; Han, B.; Chen, S.; Yang, W. Dynamic monitoring of soil salinization in Yellow River Delta utilizing MSAVI-SI feature space models with Landsat images. *Environ. Earth Sci.* **2019**, *78*, 1–10. [CrossRef]
78. Wei, H.S.; Wang, J.L.; Cheng, K.; Li, G.; Ochir, A.; Davaasuren, D.; Chonokhuu, S. Desertification Information Extraction Based on Feature Space Combinations on the Mongolian Plateau. *Remote Sens.* **2018**, *10*, 17. [CrossRef]
79. Wang, F.; Ding, J.; Wu, M. Remote sensing monitoring models of soil salinization based on NDVI-SI feature space. *Trans. Chin. Soc. Agric. Eng.* **2010**, *26*, 168–173. [CrossRef]
80. Ding, J.; Qu, J.; Sun, Y.; Zhang, Y. The retrieval model of soil salinization information in arid region based on MSAVI-WI feature space:A case study of the delta oasis in Weigan-Kuqa watershed. *Geogr. Res.* **2013**, *32*, 223–232.
81. Jagdhuber, T.; Hajnsek, I.; Bronstert, A.; Papathanassiou, K.P. Soil Moisture Estimation Under Low Vegetation Cover Using a Multi-Angular Polarimetric Decomposition. *IEEE Trans. Geosci. Remote Sens.* **2013**, *51*, 2201–2215. [CrossRef]
82. Bourgeau-Chavez, L.L.; Leblon, B.; Charbonneau, F.; Buckley, J.R. Evaluation of polarimetric Radarsat-2 SAR data for development of soil moisture retrieval algorithms over a chronosequence of black spruce boreal forests. *Remote Sens. Environ.* **2013**, *132*, 71–85. [CrossRef]
83. Yang, J.; Zhao, J.; Zhu, G.; Wang, Y.; Ma, X.; Wang, J.; Guo, H.; Zhang, Y. Soil salinization in the oasis areas of downstream inland rivers—Case Study: Minqin oasis. *Quat. Int.* **2020**, *537*, 69–78. [CrossRef]
84. Feng, J.; Jing, J.; Wei, W. A Study of soil salinization in Weigan and Kuqa rivers oasis based on Albedo-MSAVI feature space. *China Rural Water Hydropower* **2018**, *2*, 147–152.
85. Gao, Y.; Liu, X.; Hou, W.; Han, Y.; Wang, R.; Zhang, H. Characteristics of Saline Soil in Extremely Arid Regions: A Case Study Using GF-3 and ALOS-2 Quad-Pol SAR Data in Qinghai, China. *Remote Sens.* **2021**, *13*, 417. [CrossRef]